Materials Horizons

ROYAL SOCIETY OF CHEMISTRY

COMMUNICATION

Cite this: *Mater. Horiz.*, 2022, 9, 2581

Received 31st March 2022,
Accepted 18th July 2022

DOI: 10.1039/d2mh00403h

rsc.li/materials-horizons

Self-strengthening tape junctions inspired by recluse spider webs†

Ben H. Skopic, Sean R. Koebley and Hannes C. Schniepp *

Adhesive tapes are versatile and widely used yet lack adhesion strength due to their tendency to fail *via* peeling, a weak failure mode. A tape with surprising adhesive properties is the recluse spider's 50 nm-thin silk ribbon with a 1 : 150 aspect ratio. Junctions of these microscopic sticky tapes can withstand the material's tensile failure stress of ≈1 GPa. We modeled these natural tape–tape junctions and revealed a bi-modal failure behavior, critically dependent on the two tapes' intersection angle. One mode leads to regular, low-strength peeling failure, while the other causes the junction to self-strengthen, eliminating the inherent weakness in peeling. This self-strengthening mechanism locks the two tapes together, increasing the junction strength by 550% and allowing some junctions to remain intact after tensile failure. This impressive adhesive strength of tapes has never before been observed or predicted. We found that recluse spiders make tape junctions with pre-stress to force the locked, high-strength failure mode. We used this approach to make junctions with synthetic adhesive tapes that overcame the weak peeling failure.

New concepts

Adhesion of sticky tapes is usually weak because stress concentrates at a peeling front, akin to crack propagation in bulk materials. Through studying the toughness enhancing mechanical metastructures that recluse spiders build into their tape-based webs, we discovered a self-strengthening mechanism in junctions of two adhesive tapes. Under tensile load, these tape junctions can remain intact past the failure point of the tapes themselves: a strength threshold never before reported in any tape–tape junction. When optimized, these junctions prevent the formation of a peeling front, eliminating the inherent weakness of peeling mode failure. Our findings can readily be observed with common adhesive tape—or exploited for bio-inspired applications and designs, such as novel composites and other, additively manufactured tape-based materials systems.

Introduction

Adhesives relying on van der Waals (vdW) forces are reversible and instantly effective without any chemical curing process on practically any surface without the use of toxic solvents.[1–4] Engineered systems that rely on these forces include adhesive tapes with applications ranging from everyday tasks[5] to the production of graphene[6] and manufacturing of microelectronic,[7,8] and microfluidic[9] devices, fiber reinforced composites,[10–12] and layered/laminated composites.[13,14] In recent decades, bioinspiration from gecko feet,[1,15–17] insect exoskeletons,[18] and nacreous mollusk shells[19,20] have deepened our understanding of the impressive benefits of vdW adhesion. To create strong adhesion using vdW forces, these engineered and biological systems make molecular-scale contact between surfaces, often mediated through an adhesive thin film. Mechanical failure of these adhesive junctions is dominated by the low-strength mode-I ("peeling") failure.[21–23] The weakness of this failure mode is due to stress concentration at the peel front,[24,25] and consequently, tapes and other thin films are rarely used in structurally critical applications. By applying force at a small angle relative to the surface the tape adheres to, the weakness of peeling failure is mitigated resulting in enhanced adhesion as demonstrated by the gecko foot.[26,27] However, even in the zero-degree case where the force acts parallel to the substrate and the tape behaves as a lap shear joint, this strength enhancement is limited by a critical peel force where the lap shear joint breaks down due to the viscoelastic properties of the adhesive layer and begins to peel.[5,28,29]

A natural, tape-based materials system that does not exhibit the weakness associated with peeling is the recluse spider's sticky tape silk[30,31] seen in Fig. 1. This 50 nm-thin tape silk features a thickness-to-width aspect ratio (AR) of 1 : 150 and can conform perfectly and thus adhere to any surface, including itself. The tape lacks an adhesive coating,[31] relying solely on the silk's intrinsic vdW interactions to generate adhesion. The adhesion allows the spider to form a metastructure with sacrificial loops

Applied Science Department, William & Mary, P.O. Box 8795, Williamsburg, VA, 23187-8795, USA. E-mail: schniepp@wm.edu

† Electronic supplementary information (ESI) available. See DOI: https://doi.org/10.1039/d2mh00403h

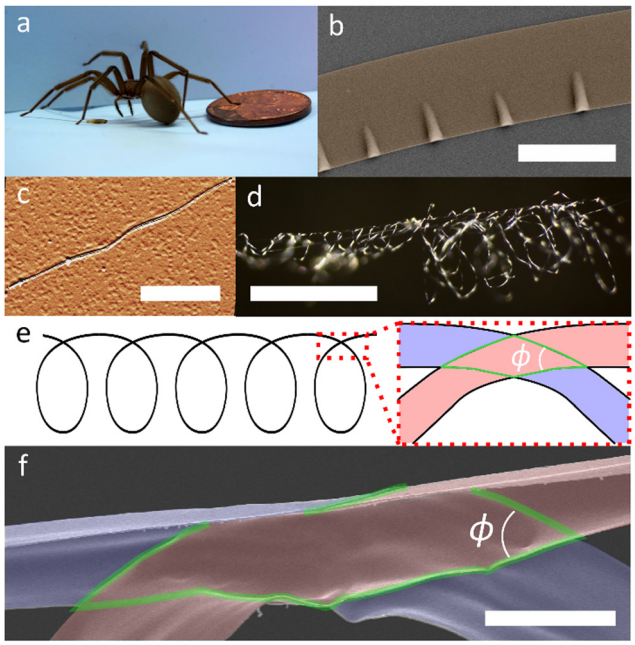

Fig. 1 (a) Adult female recluse (*L. laeta*) spider next to a penny. (b) *L. laeta* silk with ripples caused by bending of the tape (aspect ratio (AR) 1 : 150; false colored scanning electron microscopy (SEM); scale bar 10 μm). (c) Atomic force microscopy (AFM) magnitude image of the cross-section of a *L. laeta* silk fiber embedded in epoxy (scale bar 5 μm). (d) Optical image of many *L. laeta* silk loops in series (scale bar 500 μm). (e) Sketch of recluse loops in series (left) and a single loop junction (right). In the junction, the tape on top is red, the tape underneath in blue, and the junction area outlined in green with junction angle ϕ. (f) Single loop junction (SEM, false colored according to the scheme in (e); scale bar 5 μm).

from this tape silk (Fig. 1d and e) that significantly increases the toughness by way of strain-cycling.[32,33] The enhancement is only possible because the tape–tape loop junctions (Fig. 1e and f) offer impressive strength, allowing some of them to remain intact even after the tape has reached its tensile failure stress of ≈1 GPa.[32] In the adhesive junction, this corresponds to shear stresses of ≈4.5 MPa—comparable to setae on a gecko's foot.[15,16] This high strength and ability to experience tensile failure before adhesive failure has never before been reported in adhesive tape junctions, even in a zero-degree peeling configuration, and is unusual and surprising.

To study this phenomenon, we mimicked the geometry of the recluse loop junctions (Fig. 1e and f) at much larger scales with common adhesive tape and indeed observed junction failure strengths much larger than expected from peeling failure. Subsequently, we systematically studied these adhesive tape junctions and found that the azimuthal angle, or the angle at which two tapes intersect, ϕ, introduces an additional degree of freedom that plays a critical role for the failure behavior. We observed that the junctions randomly fail in one of two distinct modes: the first mode is dominated by peeling and, therefore, has low breaking strengths; the second failure mode surprisingly features a much higher breaking strength, enhanced by up to 550% for certain angles ϕ. This enhancement is possible because these thin and flexible tape junctions feature an impressive self-strengthening effect that prohibits peeling. We developed a general three-dimensional (3-D) model that successfully describes the behavior of such junctions made from any material with a tape-like morphology.

We applied our model to further understand the recluse loop junctions. We measured the junction angle and opening strength of natural loops to compare to the predictions of our model. We found that the recluse spider makes its loop junctions in a range of junction angles optimized for strain-cycling, maximizing web toughness. Through our analysis and modeling of the self-strengthening effect for tapes, we show the potential for our work to be a tool to optimize future spider silk-inspired tape-based materials and metamaterials.[13,34–38]

Results and discussion

There are countless examples where a natural materials system has unique properties not achieved by engineered materials. Here we showcase the recluse spider's tape silk that has adhesive properties never before observed or replicated in man-made tapes. To quantify this impressive adhesion, we first measured the magnitude and distribution of individual junction's strengths. We conducted tensile tests of 26 segments of naturally looped silk collected from recluse spiders, with two data sets shown in Fig. 2a. In both data sets, there are force peaks followed by a steep decrease in force, often to zero force, representing loop opening events. At each of these events, a critical force level is met and one loop junction fails. This releases additional silk stored in the loop, leading to the relaxation of the tested specimen. Only after recovering this excess length does the force begin to increase again. The height of each peak is thus a measure for the strength of the loop junction. In Fig. 2a, the first two junctions were weak and failed at a low force of 25 μN or 5% of the recluse silk's average tensile strength (TS) (indicated with green arrows). This was followed by a much stronger junction failing at ≈0.18 mN, 35% of the TS. This particular sample ultimately failed at 0.5 mN, corresponding to a TS of 0.95 GPa. The silk in the orange curve experienced two loop opening events, both at high force, with the higher one at 80% of the TS. On average, we determined that the loop opening strength of natural recluse silk is 36% of the silk's TS as shown in Fig. 2b. (Junctions failing at >100% TS are from individual samples that failed at a greater than average TS.) In addition to the junctions that opened before tensile failure, there were unopened loops after tensile failure, indicating that these junctions were even stronger than the TS. Hence, these tape–tape junctions are remarkably strong, uncharacteristic of other tape-based adhesive junctions.

To further investigate this surprisingly strong adhesion,[30–32] we used scanning electron microscopy (SEM) to quantify the geometry of the tape–tape junctions. In particular, we determined the angle ϕ at which two sections of the same silk thread intersect to form each loop (Fig. 1e). Interestingly, their junction angles were narrowly distributed at $\phi_L = 22.56^\circ \pm 5.40^\circ$

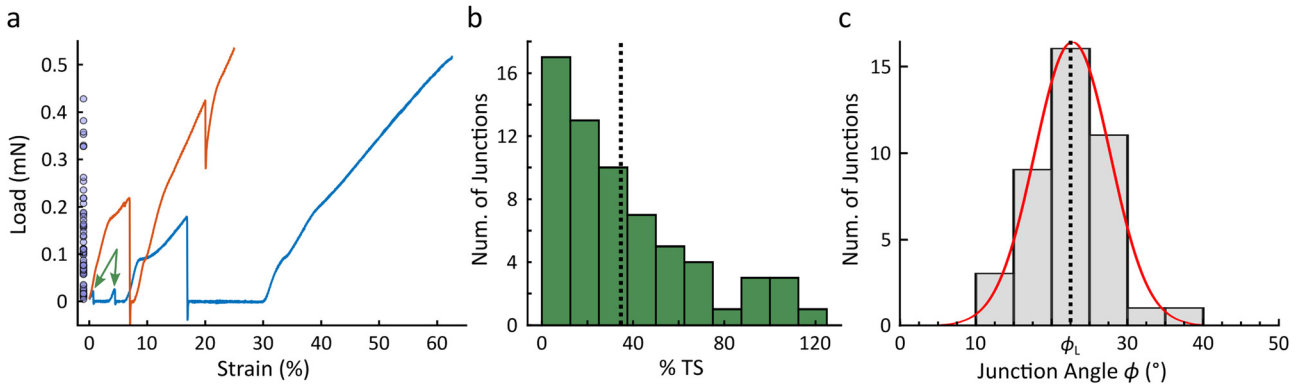

Fig. 2 (a) Two representative tensile curves of looped recluse silk. The junction strengths from all tested samples are indicated by blue dots near the vertical axis. (b) Histogram of all the recluse loop junction strengths normalized by the average tensile strength (TS) of recluse silk. The average junction strength is indicated with a dotted line. (c) Distribution of loop junction angles observed in natural recluse spider silk (grey histogram, with the vertical solid black line labeled ϕ_L representing the mean). The red curve represents the continuous distribution of the measured loop junction angles.

($N = 41$) as shown in Fig. 2c. It is interesting and surprising that from this relatively narrow range of junction angles, we observed a broad range of junction strengths corresponding to 1.5–100% TS of the silk itself.

To explore the 3-D failure mechanics resulting from this tape–tape junction geometry and the introduction of the azimuthal angle ϕ, we used Scotch® tape as an experimental model system. This tape has a width of 12.7 mm and an AR of 1 : 220,[39] which mimics the aspect ratio of recluse tape silk (Fig. 1) closely, albeit scaled up by a factor $\approx$2000.

We systematically varied the tape–tape junction angle, ϕ, and applied a tensile force, F, on each of the joined tapes as illustrated in Fig. 3a (forces indicated by red and blue arrows) to record its tensile response. Our experimental results in Fig. 3b revealed that the junction angle had a strong, and in some areas, highly critical influence on the observed strength of the junction. Due to the geometry of this system, the area of the junction diverges as the junction angle approaches zero. To investigate the influence of the junction angle independent of its effect on the junction area, we normalized our tensile results in Fig. 3b by the junction area. Specimens with junction angles $\phi \leq 20^\circ$ have a junction area so large that they exhibit tensile failure of the tape rather than failure of the junction (region I). Correspondingly, these data points follow the black, dashed line representing the tape's TS normalized by its junction area. For angles $\phi > 20^\circ$, the results exhibit significant scatter, however, all data showing a clear lower border (green curve in Fig. 3b). For $20^\circ < \phi \leq 32^\circ$, this lower border falls rapidly (region II) and for $\phi > 32^\circ$, the lower border slowly decreases as ϕ increases (region III). This behavior, with several distinct regions, especially the significant strength enhancement for particular angles, has not been previously described and merits further investigation in detail.

Our detailed study of the underlying mechanisms for this peculiar junction failure behavior involved video analysis of the tensile tests—see ESI† for the compiled video "Side-by-Side Video Comparison.mp4"‡—which revealed that samples with larger junction angles (region III) predominately separated by

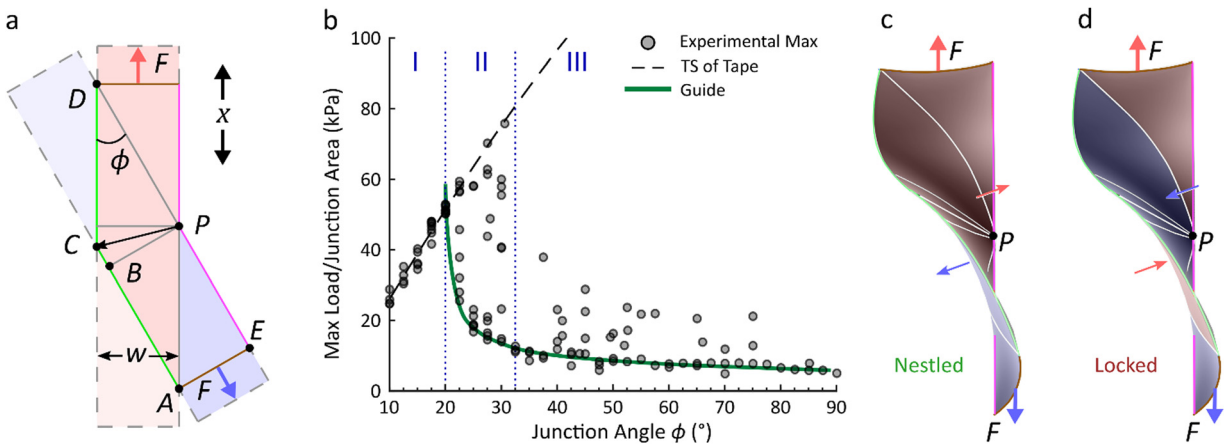

Fig. 3 (a) Tape–tape junction schematic with ϕ = 30°. The red/blue shadings represent the top/bottom tapes, respectively. (b) The experimental strength normalized by junction area as a function of junction angle. Three failure regimes are marked by roman numerals. (c) Depiction of junction area buckling into the "nestled" shape, allowing peeling. (D) "Locked" conformation leading to the cusp and elastic strain. The regions outlined with gray dashed lines in (a) are not shown in (c) or (d).

peeling. Since peeling progresses at low force, these junctions are relatively weak. Decreasing the junction angle (region II) leads to a moderate increase of the junction area, yet we observed a fundamental change in the failure mode. Notably, we found that the junctions in region II exhibited elastic stretching rather than peeling, similar to a lap shear scenario,[40,41] leading to junction strengths up to 1300% higher than in region III. In some cases in regions I and II, the junctions were—despite relying on the same adhesive system—strong enough that the tapes reached their TS and experienced tensile failure rather than junction failure (points along the dashed line).

Geometric description

Our video analysis (see ESI†) also revealed that the tape–tape junctions assumed a non-trivial, 3-D conformation. Originally, the junction is in a flat configuration of two tapes (Fig. 3a), where the pink lines on the right side of the tapes make a distinct angle. The application of force F at the two ends of the junction as shown with the respectively colored arrows in Fig. 3a effectively works to bring the two pink lines into one straight line (Fig. 3c and d). Because the green line AC is longer than the pink line EP by a difference of BC, as shown in Fig. 3a, the green side of the junction buckles, introducing a 3-D curved shape shown in Fig. 3c and d. Due to the high AR of tapes, the energy absorbed in this buckling process is negligible. Assuming that the tapes are originally in a relaxed position without twists, there are two possible minimum energy conformations of this buckling that can occur. The two conformations caused by the buckle form by moving excess length either out of plane or into plane based on the perspective of Fig. 3a. Because of the stacking order of the tapes, these two conformations lead to significantly different behavior.

One of these conformations, the into-plane buckle, effectively leads to the two tapes being nestled together, only being held together by the adhesive (Fig. 3c), while the other conformation, the out-of-plane buckle, locks the two tapes together (Fig. 3d). In both conformations, the applied tensile forces have components normal to the junction area introducing equal and opposite forces between the two tapes in the buckled region (smaller red and blue arrows in Fig. 3c and 3d). Using the stacking order of the tapes, if the junction buckles into the "*nestled*" conformation as shown in Fig. 3c, these forces are directed such that the two tapes are pulled apart and the junction goes directly into peeling mode failure. However, if the junction buckles into the "*locked*" conformation as shown in Fig. 3d, the equal and opposite forces press the two tapes against each other, forming a stable cusp. This locked conformation is particularly interesting because it leads to a natural self-strengthening effect where the applied load effectively holds the tapes together. Peeling is inhibited, and the tapes are elastically strained instead.

These two buckling conformations lead to a vastly different mechanical response although the physical adhesive system remains the same. At a fundamental level, adhesion in most tapes is provided by vdW forces, which are intrinsically weak. Furthermore, tape delamination is dominated by mode-I peeling failure, which concentrates stress at the peel front. Hence, these adhesive systems are weak for two independent reasons. The strength enhancement provided by the peeling inhibition described here is thus particularly important for any vdW-based adhesive tape.

Peeling model

Peeling is observed if the junction assumes the nestled conformation and can be described as follows. The force required to drive the peeling process is proportional to the width of the peeling front. The peeling front is perpendicular to $\overline{PC}$ and propagates across the junction area (the rhombus PACD) along $\vec{PC}$ until the two tapes separate (see Fig. 3a and Fig. S1, ESI†). The progression of peeling effectively adds length to the specimen in the tensile direction, x. The maximum tensile length added is x_{max} and is defined as follows:

$$x_{max} = 2w \tan\frac{\phi}{2}, \tag{1}$$

where w and ϕ are the width of the tape and the junction angle respectively. Since we apply and measure the force in the tensile direction, which is not the same direction that peeling propagates, we consider the peeling force, F_p, as a function of x. As peeling progresses, the peeling force, $F_p(x)$, first linearly increases, according to the shape of the junction area. It peaks when $x = x_{max}/2$, then linearly decreases symmetrically and can thus be expressed as:

$$F_p(x) = 2\gamma \csc^2\left(\frac{\phi}{2}\right)\cot\left(\frac{\phi}{2}\right)\cdot\begin{cases} x & 0 \le x \le \dfrac{x_{max}}{2} \\ (x_{max} - x) & \dfrac{x_{max}}{2} \le x \le x_{max} \end{cases}, \tag{2}$$

where γ is the experimentally obtained phenomenological adhesive energy of the two tapes. (Complete derivation in ESI.†) In this pure peeling regime, we assume that the straining force of the tape can be neglected and all of the force goes into separating the two tapes *via* peeling (see ESI† for details).[24,42]

To test whether eqn (2) correctly predicts the progression of the forces during the peeling process, we compare it to our experimental results using measured parameters for the Scotch® tape (see ESI†). In Fig. 4 we plot experimental results (solid colored lines) for three different junction angles, including both buckling conformations, and the predictions of the peeling model (eqn (2), purple dashed lines). The solid purple curves in Fig. 4 are identical and show the maximal forces normalized by the junction area sustained in a pure peeling failure as a function of ϕ. The experimental data for a junction with $\phi = 42.5^\circ$ in the nestled conformation (Fig. 4a) is in good agreement with our prediction according to eqn (2). The experimental maximal force in Fig. 4a closely matches the solid purple curve as marked with a solid purple dot. However, the maximal force for a junction with $\phi = 57.5^\circ$ in locked conformation (Fig. 4b, red dot) is much higher than the maximal force predicted for an identical junction failing by pure peeling (solid purple dot). This is an example where a model based only on peeling does not describe all our experimental evidence

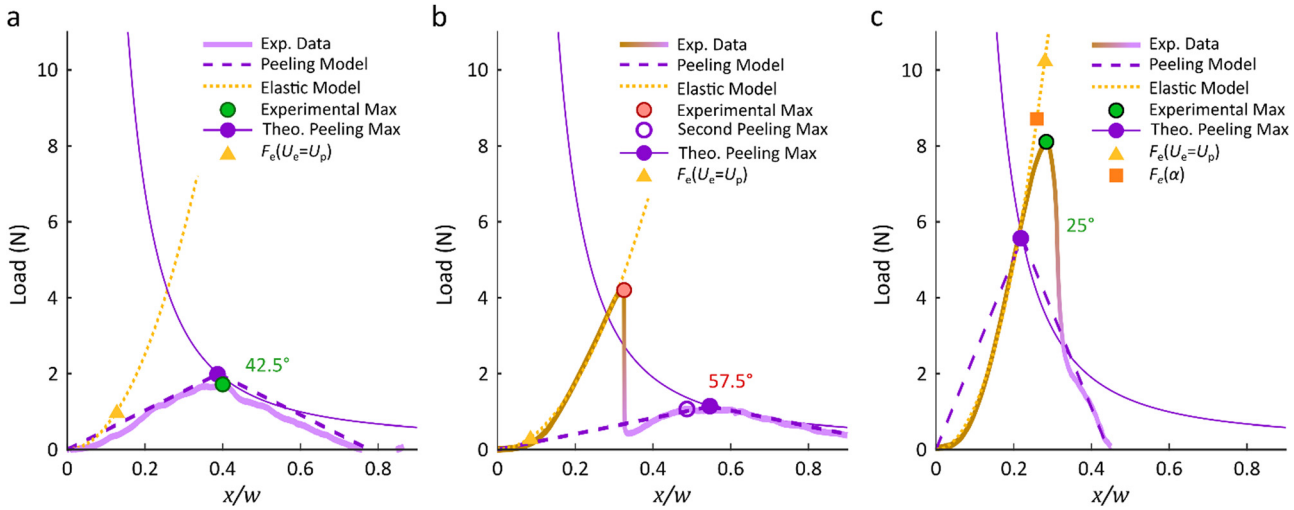

Fig. 4 Three characteristic tensile curves to validate peeling and elastic Models. Experimental tensile data (solid curves) from three representative junctions with junction angles 42.5° (a, nestled), 57.5° (b, locked), and 25° (c, nestled). The tensile displacement x, normalized by the width w. Dashed and dotted curves are derived from eqn (2) and (3), respectively, for each of the three featured junction angles. The location and color of the square and triangular points correspond to the yellow and orange curves in Fig. 5a.

correctly: a significant number of data points are in the locked conformation, substantially outperforming peeling mode failure with significantly enhanced adhesive performance.

Elastic model

We observed that junctions with enhanced adhesion, such as the junction with $\phi = 57.5^\circ$ in Fig. 4b, were initially in the locked conformation, forming a cusp. In this conformation shown in Fig. 3d, peeling is prevented by the tapes being pressed against each other, causing the tapes to be elastically strained instead. The pink line on the junction in Fig. 3d is initially the only straight line in the tensile direction and, therefore, is initially the only material being strained while the rest of the junction is still buckled and relaxed. As the external force increases, areas neighboring the pink line also get exposed to strain, and thus the strained area becomes wider, with the highest strains on the pink side of the junction area. This asymmetric straining progressively flattens the junction area with more length added to the pink side, reducing the buckled area. This behavior of the buckled junction is described by the first case of the following equation:

$$F_e(x) = \begin{cases} \dfrac{-1}{2} Etx \tan(\phi) \ln\left| \dfrac{2x}{\beta \tan\left(\dfrac{\phi}{2}\right) \tan\phi} - 1 \right| & 0 \le x \le \alpha \\ wE(x-\alpha) + F_e(\alpha) & x \ge \alpha \end{cases}, \quad (3)$$

where E is the Young's modulus of the tape, t is the thickness of the tape, and β is the total length of the sample. (Complete derivation in ESI.†) Our experiments showed that once a sufficient portion of the junction area had been strained flat, the slope of $F_e(x)$ became approximately linear (Fig. ESI†), which is modeled by the second case of eqn (3) and is determined by the width, w, and the Young's modulus, E, of the tape. This transition occurs when $x = \alpha$, where α is defined as the point where the slope of the first case reaches wE. Eqn (3) is plotted for each of the corresponding junction angles in Fig. 4 as a yellow, dotted curve. Eqn (3) only considers a linear-elastic material response and no shear forces within the junction. Additionally, eqn (3) assumes that the center of the junction is located at $\beta/2$; see ESI,† for our detailed assessment of these assumptions.

For comparison with our experimental data we used the experimentally determined parameters for Scotch® tape (see ESI†). We found that this description of the elastic mode is indeed in excellent agreement with the curves featuring enhanced adhesion, which could not be explained with a peeling failure. The accuracy of our elastic model is demonstrated by the 57.5° sample in Fig. 4b and the 25° sample in Fig. 4c, where the junction originally very closely follows the predicted elastic mode (dotted yellow curve). However, in Fig. 4b at the red dot, the curve reaches its force maximum, after which it sharply drops. The force corresponding to the red dot is significantly above the maximum force (solid purple dot) predicted by the peeling model for 57.5° (dashed purple line). Thus, the locked conformation and corresponding elastic load response is the reason this curve featured a breaking force significantly above the prediction of the peeling model. We found that all specimens in region III featuring enhanced junction strength were in line with this elastic mode in a similar way. This suggests that the observed junction enhancements in region III are due to peeling inhibition of specimens in the locked conformation.

Interestingly, the 57.5° curve shown in Fig. 4b also closely follows the peeling model predictions, indicated by purple dashed line, following the drop after its global maximum (red dot). For the 57.5° curve, the force reaches a second, local maximum indicated by an open purple dot. This local maximum is close to the

maximum predicted by the peeling model (closed purple dot). Accordingly, all specimens in region III featuring enhanced adhesion (red dots in Fig. 5a) due to the initial locked conformation, transitioned into peeling failure with second maxima (open purple dots in Fig. 5a) in line with the peeling model (purple curve in Fig. 5a). This implies that this transition from the elastic to peeling mode occurs at a tensile displacement before the peeling maximum is reached ($x < x_{max}/2$), meaning that the junctions peel through a local maximum at $x_{max}/2$ until the tapes separate at x_{max}. The 25° sample shown in Fig. 4c also transitions from the elastic to the peeling mode; however, the transition happens at a displacement larger than the predicted maximum of the peeling mode (purple dot at $x/w \approx 0.2$). While the experimentally observed curve is still in excellent agreement with the peeling model for $x/w > 0.35$, there is no second maximum. A remaining question is at what point the transition between the elastic mode and the peeling mode occurs.

Energetic description

To understand the transition between stretching and peeling, we have to consider the energies U_e and U_p associated with the elastic and peeling failure modes, respectively—thus far, only forces have been discussed. In Fig. 4, we plot peeling and elastic theoretical force curves for three junction angles with representative raw tensile data. The energy, *i.e.* work, is determined by taking the integral of the respective force functions with respect to x or the area under the theoretical curves. At the onset of tensile force, regardless of the junction angle, the elastic force has a zero slope, whereas all peeling curves feature a constant positive slope. Thus, the elastic mode is initially favored because it requires less force and energy ($F_e < F_p$ and $U_e < U_p$). As the tensile displacement increases, the elastic force will become greater than the peeling force and lead to much higher forces than the peeling model predicts ($F_e > F_p$). Therefore, one might wonder whether this would permit the system to switch from the elastic mode to the peeling mode of failure. For that to happen, the stored elastic energy would have to be used to separate the two surfaces through a degree of peeling with an equivalent tensile displacement. However, at this point, the energy stored in the tape by stretching is still less than the surface energy required to open the junction by peeling ($F_e > F_p$ and $U_e < U_p$), and therefore, a spontaneous transition from the elastic into the peeling mode is prohibited. This allows the junction to experience forces much greater than the predicted maximum peeling force. The transition becomes energetically favorable at a higher displacement, once the peeling and elastic energies become equal ($U_e = U_p$) marked by yellow triangles in Fig. 4. In Fig. 5a we determined the elastic force where the energies of both modes become equivalent ($F_e(U_e = U_p)$) as a continuous, yellow curve as a function of the junction angle. Having considered geometries, forces, and energies, we are now prepared to understand why the behavior in regions I, II, and III is so different.

For junctions in region III, energy equivalence occurs at small displacements. Therefore, in the nestled conformation (Fig. 3c), the transition into the peeling mode happens at such small displacements and forces that it is undetectable, as shown with the 42.5° curve in Fig. 4a. However, if the junction is initially in the locked conformation (Fig. 3d and the 57.5° curve in Fig. 4b), peeling is geometrically prevented, and the junction remains in the elastic mode for longer than energetically predicted. As shown with the pairs of red and open purple data points throughout region III in Fig. 5a, all these junctions eventually transition into peeling.

As the junction angle decreases towards region II, the yellow curve in Fig. 5a increases, meaning that the junctions will remain in the elastic mode for larger displacements and larger forces for energetic reasons. Region II is differentiated from region III by the intersection of the yellow and purple curves at $\phi_{II,III} = 31.8°$. When junctions with junction angles less than

a

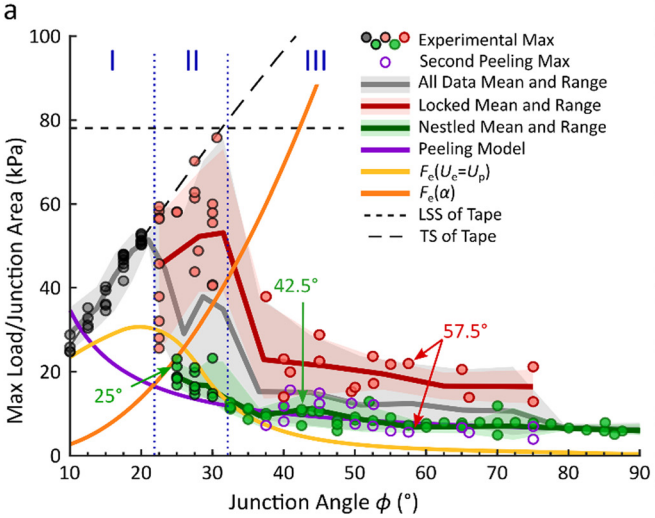

b

Region	Conformation	Data Point/ Constraints	Strength Enhancement	Failure Mode
III	Nestled		None	Pure peeling
	Locked		Moderate	Self-strengthen ⇒ peeling
II	Nestled		Moderate Minimal	Mixed-mode (energy limited)
	Locked		Maximal Significant	Self-strengthen (peeling prohibited)
I	Both		Maximal	Lap shear/tensile failure (flattened junction)

Fig. 5 (a) Experimental data from Fig. 3b with the peeling (purple), elastic (orange), and energetic (yellow) models overlayed. The red and green arrows indicate the three cases highlighted in Fig. 4. Since the data is normalized by the junction area, the tensile strength (TS) changes with ϕ, whereas the lap shear strength (LSS) automatically appears constant in this case. (b) Table of all possible failure modes of a single tape–tape junction.

$\phi_{II,III}$ reach energy equivalence, the elastic force that the junction experiences is greater than the maximum possible peeling force ($F_e(U_e = U_p)) > F_p(x_{max}/2)$). As a result, the junction will always reach a force greater than the peeling maximum, regardless of the junction's initial conformation. Even junctions initially in the nestled conformation will always fail at a force greater than the maximum force predicted by the peeling model. By delaying the junction's transition to peeling, the junction is effectively strengthened. This ''energetic strengthening'' is illustrated by the 25° curve in Fig. 4c, which falls within region II, representing a junction with an initial nestled conformation. The tensile data follows the elastic regime closely until the peeling maximum ($x = x_{max}/2$), where we begin to see a deviation from the elastic model. At $x_{max}/2$, less force is required to peel but the system does not yet have enough energy to spontaneously flip completely into the peeling mode. At this point, the system continues to experience increasing load through a mixed mode failure, combining partial peeling with partial stretching. Only when the junction reaches the displacement where we predict the energies to be equal (yellow triangle) does the junction make the complete transition, releasing the stored elastic energy and the junction begins to fail by the pure peeling as described by eqn (2).

This energetic strengthening of the junction is moderate, also reflected in Fig. 5a where all data points in region II are above and increasingly trend away from the purple curve as junction angles decrease. For junctions that are initially in the nestled conformation, we would expect their maximum force to be at the yellow curve. However, the mixed-mode failure causes these junctions to have slightly lower maxima that are located between the red and yellow curves.

The locked conformation leads to even more strength enhancements, represented by data points significantly above the yellow curve. These junctions in region II, still at relatively large junction angles, reach forces approaching the TS of the material and the lap shear strength (LSS) of the junction area. The LSS of a material is the force required to separate two flat adhered substrates in a pure lap shear mode, normalized by their contact area.[40,41] Junctions with the locked conformation will be elastically strained to $x = \alpha$ where the elastic force becomes linear and the once buckled junction area becomes practically flat. In this case, the forces contributing to either peeling or the cusp go to zero, thus meeting lap shear conditions. This critical point is marked by an orange square in Fig. 4c and as a continuous function of the junction angle (orange curve) in Fig. 5a. Once the junction is strained to $x = \alpha$, peeling is prohibited so that the junction behaves as a lap shear joint, achieving high strengths, limited only by the TS or LSS of the tape, marked by black, dashed lines in Fig. 5a.

A unique phenomenon that elastic films experience under tension, as observed in our video review, is the formation of compressional wrinkles that are oriented orthogonal to the tensile direction.[43–45] We suspect that this wrinkling decreases the strength of some junctions, resulting in the wide spread of failure strengths for locked junctions in region II. One possible way to overcome the weakness introduced by this effect is to tailor an uneven load profile (for instance by pre-straining the junction or by non-uniform clamping) with stress peaks at the edges, since it has been shown that such loads reduce wrinkling.[45]

Finally, we consider the boundary between regions II and I, occurring when the orange curve intersects the purple curve in Fig. 5a ($F_e(\alpha) = F_p(x_{max}/2)$), which is calculated to be at $\phi_{I,II} = 22.4°$. Junctions with angles less than $\phi_{I,II}$ will be stretched flat, eliminating any difference between the nestled or locked conformations and meeting lap shear conditions, before the transition from the elastic into the peeling through the mixed mode is possible. Consequently, the junction strength is entirely determined by the TS or LSS of the tape. For the tape we tested, the junction performance was always limited by the TS, reflected by a tight spread around the black, dashed line in region I. Past research on similar lap-shear or zero-degree peeling cases has described a critical force threshold where the two tapes effectively peel apart at a force lower than the tensile limit of the tape.[5,28,29] For the first time, we have shown that the optimization of ϕ can produce adhesive junctions that are stronger than the tapes themselves.

Forced self-strengthening junctions

While the observed self-strengthening leads to impressive strengthening of the junctions in the locked conformation, a remaining issue is that, under the above-described assembly process, only about half (52.8%) of the junctions buckle into the higher-strength, locked conformation. Because of this spontaneous selection of the buckling conformation, the strength of an individual junction cannot be predicted, which may not desirable for some applications. To address this uncertainty, we modified the junction assembly process in a way that caused the junctions to prefer the locked conformation. This was achieved by assembling the junctions on a cylindrical surface (Fig. S4, ESI†), which effectively made one of the tapes slightly longer than the other, introducing a ''pre-buckle''. This pre-buckle caused the junction to favor the locked conformation. We express the degree of pre-buckle as $G(\phi)$, which is dimensionless, inversely proportional to the radius of the cylinder, and proportional to the width of the tape (see ESI†). We assembled junctions of our adhesive tape on two cylinders with radii $R_1 = 101.6$ mm and $R_2 = 66.0$ mm corresponding to pre-buckle factors G_1 and G_2, respectively. The radii were selected such that $R_1 = 1.5 \cdot R_2$, resulting in $1.5 \cdot G_1 \approx G_2$. Because region I is unaffected by the two buckling conformations, we only tested the effect of pre-buckling in regions II and III. The results are shown in Fig. 6.

By pre-buckling the junctions to favor the locked conformation, we significantly increased the percentage of junctions in the locked conformation and therefore also increase the strength. The G_1 pre-buckle caused 76% of junctions to self-strengthen in the locked conformation corresponding to a 18% increase in average junction strength. Decreasing the radius of the cylinder and thus increasing the pre-buckle factor, G_2 resulted in 93% of junctions self-strengthening, corresponding to a 27% increase in average junction strength. For some angle ranges such as $50° \leq \phi \leq 90°$ and around 25°, we observed that

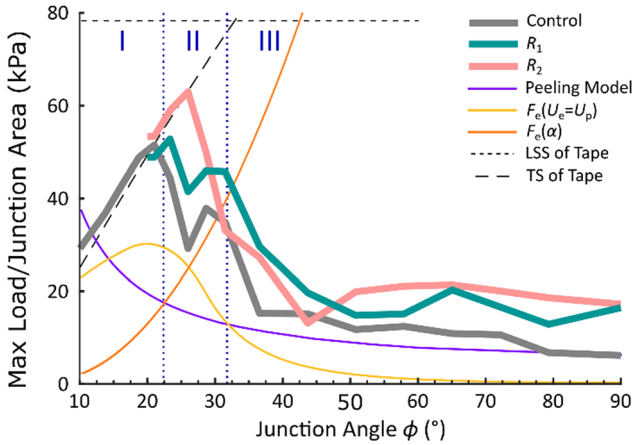

Fig. 6 Comparison of the average junction strength for both pre-buckled junction constructions (R_1 = 101.6 mm and R_2 = 66.0 mm) to the average of the junctions without any pre-buckle (control). The orange, yellow, purple, and black dashed model curves as well as the grey control curve are identical to Fig. 4.

the average junction strength increased by over 100%. Our data show that we can predictably create self-strengthening tape–tape junctions. Peeling is usually the dominating failure mode for tapes and is inherently a low-strength failure mode because of the stress concentration at the peel front. We showed that by pre-buckling the junction into the locked conformation, this weakness can be virtually eliminated. The locked conformation presses and holds the tapes together, prohibiting any crack to form or propagate between the two tapes. This allows the junctions to self-strengthen and exhibit remarkably high strength uncharacteristic of tapes.

Recluse loop junctions

We next tested whether the extremely high strengths observed in some of the recluse's loops can be successfully explained by our model. In Fig. 7a, we plotted our model using the geometric and material properties of recluse's tape silk: peeling (purple), elastic force at energy equivalence (yellow), elastic force at linearization (orange), and TS (black dashed). Using our predictive model of the loop junction failure strength as a function of the junction angle and our measured distribution of recluse loop junction angles (red bell curve), we simulated the average junction strength of the natural loops. First, we randomly generated a set of 1000 loop junction angles according to the continuous distribution (red curves in Fig. 2c and 7a) determined from our measured loop junction angles. We then assigned the junction angles in regions II and III to be in either the locked or nestled conformation based on a 50% probability (no pre-buckle). Our model predicts allowed and forbidden regions of failure strength based on junction angle and buckling conformation (see Fig. 5b). Correspondingly, we randomly assigned a failure strength to each simulated junction strength within the allowed range. Over 100 iterations of this simulation of 1000 loops, we determined the average junction strength to be 120 μN or 24% of the TS.

This result is significantly smaller than our measured average loop junction strength, 36% of the TS. This discrepancy caused us to suspect that pre-buckling is implemented in the recluse silk metastructure. Correspondingly, we altered our simulation to incorporate a pre-buckle and found that when we assigned 85% of the junctions to the locked conformation, we obtained the experimentally observed junction strength of 36% of the TS. This set of simulated data points are plotted in Fig. 7a and colored according to Fig. 5b. Thus, according to our model and simulation, the spider must pre-buckle each of its loop junctions to match the average junction strength we measured. We indeed observed a curvature in all SEM images of the natural loop junctions as demonstrated by Fig. 1f and 7b, c. This curvature indicates that the recluse spiders pre-buckle their loop junctions, forcing each junction into the locked

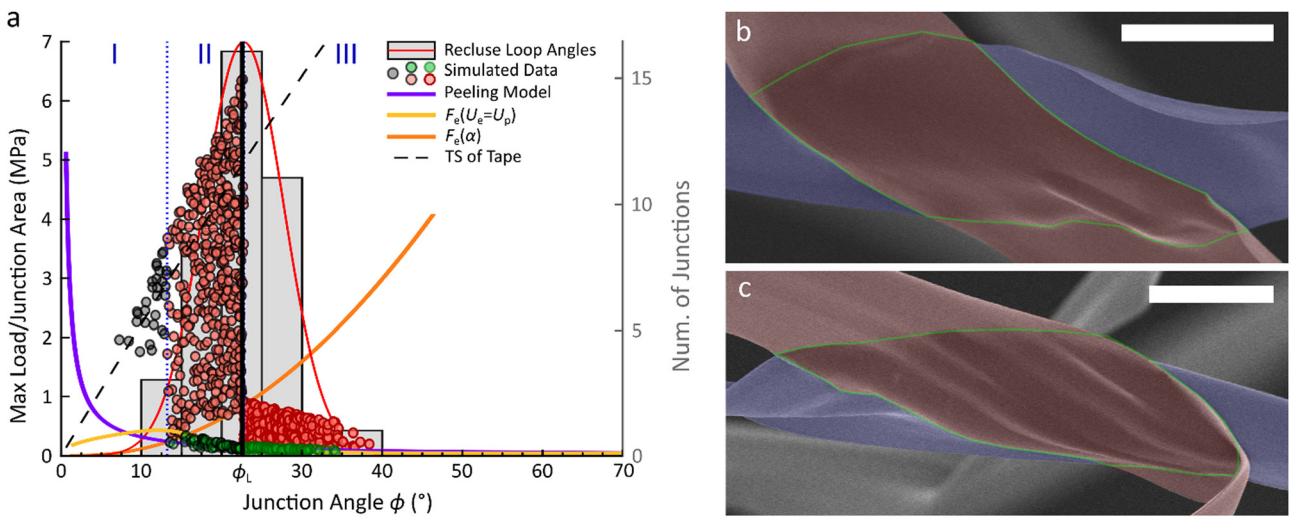

Fig. 7 Modeling & visualizing pre-buckled recluse spider's loop junctions. (a) The purple, yellow, orange, and black dashed curves are from our model, adapted to the adhesive and mechanical parameters of recluse silk (see ESI†). Histogram, red curve, and vertical black line are from Fig. 2c. The data points represent one iteration of our simulation. (b and c) Recluse loop junctions showing a pre-buckle (SEM; scale bars: 5 μm).

conformation and allowing each junction to self-strengthen. Therefore, the recluse spider naturally makes tape–tape junctions that prevent peeling.

Koebley *et al.*[32] determined that the loop system's mechanism for toughness enhancement is a mechanical "strain-cycling" phenomenon, where opening of a loop junction releases the length "hidden" in the loop, reducing strain in the fiber.[32,33] Continued straining will lead to an increase in the stress again until the next loop junction opens as shown in Fig. 2a. Each of these events adds another peak to the stress–strain curve and thus increases the area under the curve, *i.e.* its toughness. This toughness enhancement is maximized when the number of these loop opening events is maximal and the junction strengths are broadly distributed. In contrast, if all junctions failed at the same high strength, all junctions would open simultaneously, preventing the cyclic behavior and toughness enhancement. Having a relatively broad distribution of junction strengths thus improves the mechanical properties of the thread.

According to our model and using previously measured parameters for the recluse's tape silk,[30,46] the boundary between regions II and III is at $\phi_{II,III} = 22.77^\circ \pm 5.34^\circ$, the boundary between regions I and II is at $\phi_{I,II} = 13.21^\circ \pm 1.98^\circ$ (see Fig. 7 and Table S1 ESI,† for details). Notably, $\phi_{II,III}$ is very close to the mean junction angle the spiders produce ($\phi_L = 22.56^\circ \pm 5.40^\circ$), corresponding to a broad distribution of junction strengths. According to the distribution of measured loop junction angles (histogram in Fig. 7a), only a very small number of loops are in region I, where the junction strength exceeds TS. This is exactly in line with our experimental observation that only a small fraction of loops did not open after tensile failure. Too many unopened loops would essentially add "dead weight" to the system and thus reduce the specific toughness. Thus, the recluse spider makes its looped web metastructure with a distribution of junction angles that is ideally adjusted to optimize the toughness of this unique natural materials system.

Recluse spiders are not the only species of spider that produces a silk with impressive adhesive properties. Most spiders implement several different adhesive solutions, such as coating their main dragline silk with a viscous adhesive coating called viscid silk, to aid in prey capture[47–49] and web construction.[50] Spiders also spin complex attachment disc structures with pyriform silk to adhere their webs to surfaces.[51–53] The existing work on spider silk adhesives has resulted in the development of many bioinspired adhesives that closely mimic the natural material and have comparable properties.[49] These natural and engineered systems enhance adhesion with complex chemistries interacting with water vapor, and with complex organization to maximize contact area with the substrate. The latter is challenging for the silk fibers with cylindrical geometry[47,52,53] and because of the molecular-scale roughness of surfaces in general.[16] In stark difference with other spider silks and commercial adhesive systems, recluse spiders do not use a dedicated, soft adhesive layer on their silk to maximize contact area. Instead, contact area is maximized through the thinness of the ribbon made from stiff and non-viscous major ampullate silk, which naturally conforms to rough surfaces. This approach has the potential to lead to stronger and more durable bioinspired adhesive innovations.

Conclusions

Recluse silk features vdW-based silk–silk junctions without any additional adhesive coating that feature a strength far exceeding what we would expect from tape peeling. To explore the origins of this surprisingly strong adhesion, we mimicked the recluse silk using Scotch® tape, which revealed that the junction angle plays a pivotal role on a junction's strength. A non-zero junction angle leads to buckling of the junction when exposed to stress. As a function of the junction angle, we observed three distinct regions with two independent failure modes that arise from opposite buckling conformations. In the nestled conformation, the junction experiences low-strength peeling failure. However, we discovered that when the junction buckles into the locked conformation, it exhibits a peculiar self-strengthening mechanism. This mechanism prohibits peeling, and thus removes the underlying cause for the weakness commonly associated with adhesive tapes and provides the junction with record strength.

We developed a model explaining the allowed failure behavior within and between the three failure regions based on geometric, energetic and material property considerations. Our model also correctly predicts the stress–strain behavior, and thus junction strength, as a function of junction angle once the buckling conformation is known. The randomness associated with buckling generally limits our ability to predict the strength of a specific junction. However, we modified our sample construction to control the buckling and practically prevent the low-strength peeling failure mode. This elimination of peeling doubled the average junction strength.

Applying our model to the recluse spider's tape silk, we determined that the spider pre-buckles each loop junction in its looped web metastructure to prevent peeling and achieve strengths greater than the TS of the silk itself despite relying solely on vdW forces. The spider also makes its loop junctions with a distribution of junction angles that is optimized for the maximum toughness of this unique natural materials system.

Peeling is intrinsically a low-strength failure mode that inhibits the strength potential of any tape. This study of the recluse spider's tape silk reveals mechanisms to prevent any tape from peeling, demonstrating that tapes have significant structural capabilities. We believe that when combined with advanced additive manufacturing techniques, tapes are poised to become commonplace in high strength and toughness adhesive applications where peeling failure is to be avoided.

Experimental

Recluse silk collection

We cared for a colony of 200 *Loxosceles laeta* spiders. They lived in individual capsules with cotton cloths to spin their web on. The adults were fed a live cricket and the babies got a live

wingless fruit fly every week. The lifespan of the spiders in the lab is 4–5 years. Silk samples were taken directly from capsules to preserve the natural looped structure. Caution: *Loxosceles laeta* is a venomous species, and precautions need to be taken to avoid accidental bites.

Recluse silk tensile tests

The 26 silk strands were mounted onto a ''C-shape'' card stock, allowing the silk to be suspended in the opening. The samples were imaged with an optical microscope to determine the initial sample length and number of loops. Once placed in the Keysight UT150 tensile tester, the ''C-shaped'' sample holder was cut open, freeing the silk between the grips. The tensile tests we conducted at 1 mm min^{-1} with a 5 N load cell.

SEM analysis of recluse silk

The recluse looped silk samples were mounted on round SEM sample holders with 12.7 mm diameter and elevated from the surface with rolls of carbon tape. The samples were then sputter coated using a Hummer® sputtering system by Anatech Ltd with an Au-Pd alloy target for 2 minutes. The loops created by the *Loxosceles* spider were closely examined using field emission scanning electron microscopy (Hitachi S-4700 FE-SEM) using a 5 kV beam voltage to avoid burning the silk. The junction angles of the loops were measured from the SEM images using the open-source image analysis software ImageJ.

Adhesive tape

The tape used throughout this study was 3M™ Scotch® Magic 810 tape.[39] The tape was comprised of a 0.038 mm thick unplasticized polyvinyl chloride (UPVC) backing with a single-sided 0.02 mm thick pressure sensitive acrylic adhesive. This tape was chosen for its comparable AR to the *Loxosceles* silk and for its availability.

Tape–tape junction tests

Tensile tests of the tape–tape junctions used a MTS C42.503 electromotive test system with a 100 N MTS load cell. The junction angles of the samples were adjusted from 10° to 90° in 2.5° steps. The samples were made by hand using a stencil of each angle on a flat surface. For the pre-buckled samples, we varied the angle from 20° to 90° in 2.5° steps, curving the stencils around two cylinders with radii R_1 = 101.6 mm and R_2 = 66.0 mm. To make the junctions, one tape was placed vertically along the axis of the cylinder and the top tape was placed on top at the prescribed angle. This method provided an accuracy for each sample of ±1°. All tensile experiments were conducted at a constant rate of 4 mm min^{-1}.

Author contributions

B. H. S. conducted all imaging, tape experiments, and modeling. B. H. S. analyzed all data and prepared it for publication. S. R. K. produced the samples for and conducted the recluse silk tensile testing. B. H. S. and H. C. S. jointly wrote the manuscript. H. C. S. advised and oversaw the project.

Data statement

All raw data and data analysis code has been made available free of charge at **https://doi.org/10.7910/DVN/Q7LTLW**.

https://dataverse.harvard.edu/privateurl.xhtml?token=fdb5f784-a0a9-4660-bf2f-b7ed59b44eff

Conflicts of interest

There are no conflicts to declare.

Acknowledgements

This work was made possible by funding through the National Science Foundation under Grants No. DMR-1352542 and DMR-1905902. HCS acknowledges equipment support from the Office of Naval Research under Grant No. N00014-18-1-2264. We acknowledge Olga Trofimova and the W&M ARC for their help with SEM imaging.

References

‡ The supplementary video, ''Side-by-Side Video Comparison.mp4,'' features a compilation of footage from failing junctions, presented side-by-side with an animated plot featuring a live correspondence with the respective tensile data, peeling model and elastic model. The selected videos cover all possibilities for junction failure as described by Fig. 5b. The filming perspectives referenced in the video ''Front View'', as featured in Fig. S1a and c, and ''Side View'', as featured in Fig. S1b and d (ESI†).

1 K. Autumn, M. Sitti, Y. A. Liang, A. M. Peattie, W. R. Hansen, S. Sponberg, T. W. Kenny, R. Fearing, J. N. Israelachvili and R. J. Full, *Proc. Natl. Acad. Sci. U. S. A.*, 2002, **99**, 12252–12256.
2 G. Huber, S. Gorb, N. Hosoda, R. Spolenak and E. Arzt, *Acta Biomater.*, 2007, **3**, 607–610.
3 B. Soltannia and D. Sameoto, *ACS Appl. Mater. Interfaces*, 2014, **6**, 21995–22003.
4 Z. L. Peng, C. Wang and S. H. Chen, *Colloids Surf., B*, 2014, **122**, 662–668.
5 Z. Zhu, Y. Xia, C. Jiang, Z. Yang and H. Jiang, *Eng. Fract. Mech.*, 2021, **241**, 107368.
6 L. R. Dickinson, D. E. Kranbuehl and H. C. Schniepp, *Surf. Innovations*, 2016, **4**, 158–166.
7 Y.-T. Yen and Y.-C. Lin, *Sens. Actuators, A*, 2007, **139**, 330–336.
8 I. V. Uvarov, *Microelectron. Reliab.*, 2021, **125**, 114372.
9 C.-W. Tsao and W.-C. Syu, *RSC Adv.*, 2020, **10**, 30289–30296.
10 L. Mencattelli and S. T. Pinho, *Composites, Part A*, 2020, **129**, 105655.
11 J. W. Pro and F. Barthelat, *Extreme Mechanics Letters*, 2020, **41**, 101042.
12 T.-T. Yao, X.-F. Zhang, W.-S. Zhang, Y.-T. Liu, Q. Liu and G.-P. Wu, *Composites, Part B*, 2021, **224**, 109218.

13 Z. Yin and F. Barthelat, *Bioinspiration Biomimetics*, 2021, **16**, 026020.
14 L. Cheng, A. Thomas, J. L. Glancey and A. M. Karlsson, *Composites, Part A*, 2011, **42**, 211–220.
15 K. Autumn, Y. A. Liang, S. T. Hsieh, W. Zesch, W. P. Chan, T. W. Kenny, R. Fearing and R. J. Full, *Nature*, 2000, **405**, 681–685.
16 B. H. Skopic and H. C. Schniepp, *JOM*, 2020, **72**, 1509–1522.
17 D. Labonte and W. Federle, *J. R. Soc., Interface*, 2016, **13**, 20160373.
18 Y. Bouligand, *Tissue and Cell*, 1972, **4**, 189–217.
19 R. Yadav, R. Goud, A. Dutta, X. Wang, M. Naebe and B. Kandasubramanian, *Ind. Eng. Chem. Res.*, 2018, **57**, 10832–10840.
20 K. Tushtev, M. Murck and G. Grathwohl, *Mater. Sci. Eng., C*, 2008, **28**, 1164–1172.
21 J. W. Hutchinson and Z. Suo, *Advances in Applied Mechanics*, Elsevier, 1991, pp. 63–191.
22 A. A. Volinsky, N. R. Moody and W. W. Gerberich, *Acta Mater.*, 2002, **50**, 441–466.
23 M. Ciccotti, B. Giorgini, D. Vallet and M. Barquins, *Int. J. Adhes. Adhes.*, 2004, **24**, 143–151.
24 K. Kendall, *J. Phys. D: Appl. Phys.*, 1975, **8**, 1449.
25 Z. Gu, S. Li, F. Zhang and S. Wang, *Adv. Sci.*, 2016, **3**, 1500327.
26 S. Gouravaraju, R. A. Sauer and S. S. Gautam, *J. Adhes.*, 2020, **97**, 1–21.
27 K. Autumn, *J. Exp. Biol.*, 2006, **209**, 3569–3579.
28 Z. Liu, H. Minsky, C. Creton, M. Ciccotti and C.-Y. Hui, *Extreme Mech. Lett.*, 2019, **32**, 100518.
29 C.-Y. Hui, Z. Liu, H. Minsky, C. Creton and M. Ciccotti, *Soft Matter*, 2018, **14**, 9681–9692.
30 H. C. Schniepp, S. R. Koebley and F. Vollrath, *Adv. Mater.*, 2013, **25**, 7028–7032.
31 Q. Wang and H. C. Schniepp, *ACS Macro Letters*, 2018, **7**, 1364–1370.
32 S. R. Koebley, F. Vollrath and H. C. Schniepp, *Mater. Horiz.*, 2017, **4**, 377–382.
33 Y. Deng and S. Cranford, *J. Appl. Mech.*, 2018, **85**, 111001.
34 K. Agarwal, R. Sahay, A. Baji and A. S. Budiman, *ACS Appl. Polym. Mater.*, 2020, **2**, 3491–3504.
35 T. Christoff-Tempesta, Y. Cho, D.-Y. Kim, M. Geri, G. Lamour, A. J. Lew, X. Zuo, W. R. Lindemann and J. H. Ortony, *Nat. Nanotechnol.*, 2021, **16**, 447–454.
36 J. Zhang, J. Kaur, R. Rajkhowa, J. L. Li, X. Y. Liu and X. G. Wang, *Mater. Sci. Eng., C*, 2013, **33**, 3206–3213.
37 H. Grefe, M. W. Kandula and K. Dilger, *Int. J. Adhes. Adhes.*, 2020, **97**, 102486.
38 D. J. O'Brien, W. K. Chin, L. R. Long and E. D. Wetzel, *Composites, Part A*, 2014, **56**, 161–171.
39 3M Scotch, 3MTM Scotch® Transparent Film Tape 600, 3M, 2009.
40 Y. Wang, X. Yang, G. Nian and Z. Suo, *J. Mech. Phys. Solids*, 2020, **143**, 103988.
41 L. F. M. da Silva, T. N. S. S. Rodrigues, M. A. V. Figueiredo, M. F. S. F. de Moura and J. A. G. Chousal, *J. Adhes.*, 2006, **82**, 1091–1115.
42 N. Padhye, D. M. Parks, A. H. Slocum and B. L. Trout, *Rev. Sci. Instrum.*, 2016, **87**, 085111.
43 E. Cerda, K. Ravi-Chandar and L. Mahadevan, *Nature*, 2002, **419**, 579–580.
44 N. Silvestre, *Engineering Structures*, 2016, **106**, 195–208.
45 Q. Huang, J. Yang, W. Huang, G. Giunta, S. Belouettar and H. Hu, *Thin Wall Struct.*, 2020, **154**, 106838.
46 J. Zhang, S. Du, A. Kafi, B. Fox, J. L. Li, X. Y. Liu, R. Rajkhowa and X. G. Wang, *RSC Adv.*, 2015, **5**, 1640–1647.
47 G. Amarpuri, C. Zhang, C. Diaz, B. D. Opell, T. A. Blackledge and A. Dhinojwala, *ACS Nano*, 2015, **9**, 11472–11478.
48 D. Jain, C. Zhang, L. R. Cool, T. A. Blackledge, C. Wesdemiotis, T. Miyoshi and A. Dhinojwala, *Biomacromolecules*, 2015, **16**, 3373–3380.
49 X. Liu, L. Shi, X. Wan, B. Dai, Y. Chen and S. Wang, *ACS Mater. Lett.*, 2021, **3**, 1453–1467.
50 G. Greco, M. F. Pantano, B. Mazzolai and N. M. Pugno, *Sci. Rep.*, 2019, **9**, 5776.
51 E. Blasingame, T. Tuton-Blasingame, L. Larkin, A. M. Falick, L. Zhao, J. Fong, V. Vaidyanathan, A. Visperas, P. Geurts, X. Hu, C. L. Mattina and C. Vierra, *J. Biol. Chem.*, 2009, **284**, 29097–29108.
52 V. Sahni, J. Harris, T. A. Blackledge and A. Dhinojwala, *Nat. Commun.*, 2012, **3**, 1106.
53 J. O. Wolff and M. E. Herberstein, *J. R. Soc., Interface*, 2017, **14**, 20160783.